Journal of Alloys and Compounds 293–295 (1999) 508–520

Advanced nanocrystalline Zr-based AB_2 hydrogen storage electrode materials for NiMH EV batteries

L. Chen[a,*], F. Wu[b], M. Tong[a], D.M. Chen[a], R.B. Long[a], Z.Q. Shang[b], H. Liu[a], W.S. Sun[a], K. Yang[a], L.B. Wang[a], Y.Y. Li[a]

[a] *Institute of Metal Research, Chinese Academy of Sciences, Shenyang 110015, People's Republic of China*

[b] *National Engineering Development Center of High-Tech Energy-Storage Materials, Zhongshan 528437, People's Republic of China*

Abstract

The metallurgical microstructure, crystal-structure and electrochemical properties of Laves phase Zr–V–Mn–Ni system alloys (modified with Ti, Co, Sn, etc.) were investigated systematically in the present paper. Conventional polycrystalline Zr-based alloys, which consist of cubic C15 Laves phase, hexagonal C14 Laves phase and non-Laves phase (such as Zr_7Ni_{10}, Zr_9Ni_{11}, $Zr(NiMn)Sn_{0.35}$), show the highest discharge capacity of 342 mAh g^{-1} (at 60 mA g^{-1} charge–discharge current), which decreases by 7.8% after 300 cycles. Amorphous phase alloys in melt-spun alloys exhibit poor electrochemical properties. Advanced nanocrystalline C15-Laves single-phase alloys were prepared by completely crystallizing the melt-spun amorphous $Zr_{1-x}Ti_x[(NiVMnCo)_{1-y}Sn_y]_{2+\alpha}$ alloys. These alloys have a special microstructure composed of high-density interface phase and random-oriented grains varying from several nanometres to several dozens of nanometres. It was found that these materials had high discharge capacity (the maximum capacity is up to 379 mAh g^{-1}) and long cycle life (the capacity only decreases 3% after 300 cycles). The maximum discharge capacities were found in the metallurgical microstructure and crystal-structure in Zr-based AB_2 alloys. The maximum discharge capacity increases in regular nanocrystalline/C15-Laves single-phase>polycrystalline/multi-phase (Laves and non-Laves)>comorphous state/C15-Laves single-phase. It was shown that the complete crystallization method from amorphous solids is an effective way to greatly improve the electrochemical performance of Zr-based AB_2 hydrogen storage electrode materials, which is not only significant for academic research but also valuable for practical applications in the NiMH battery system for pure electric vehicles (PEV) and hybrid electric vehicles (HEV). © 1999 Elsevier Science S.A. All rights reserved.

Keywords: Nanocrystalline electrode materials; Zr-based AB_2 hydrogen storage alloys; Complete crystallization method from amorphous solids; Metallurgical microstructure and crystal-structure; Electrochemical properties

1. Introduction

With the development of economics and city traffic, more and more heavy fuel-powered vehicles appeared, resulting in more serious pollution to the city environment. The development of an electric vehicle (EV) is a new developing trend in the world automotive industry and an important act for protecting the environment. Developing an advanced electric vehicle with large load capacity, high speed and long distance from a single charge is the key to the application of the electric vehicle, besides mandatory orders from governments and their legislation. A rechargeable battery with high energy density is the key to the advanced electric vehicle. Because of its various advantages, more and more research is focused on the NiMH battery used as the power system in electric vehicles [1–6]. A practical NiMH60Ah battery (specific energy of 51 Wh kg^{-1}) has been developed in the Institute of Metal Research, Chinese Academy of Sciences. This kind of battery can be successfully used for a small-sized bus (with a load capacity of four people), which can travel 100 km at a speed of 60 km h^{-1} after a single charge of the battery system. The Ovonic Battery Company (OBC) in the United States has developed a NiMH200Ah battery with a specific energy of 80 Wh kg^{-1} [7], while the primary medium term goals of the United States Advanced Battery Consortium (USABC) for specific energy is 80–100 Wh kg^{-1} [8].

It is obvious that high-capacity hydrogen storage alloys are essential to the NiMH batteries with high specific energy. Since the commercialized AB_5 alloys are limited by their relatively low hydrogen storage capacity [9,10],

---

*Corresponding author. Tel.: +86-24-23843531 ext. 55402; fax: +86-24-23891320.

E-mail address: lianchen@yeah.net (L. Chen)

0925-8388/99/$ – see front matter © 1999 Elsevier Science S.A. All rights reserved.
PII: S0925-8388(99)00476-4

Zr-based AB_2 Laves phase alloys, as a new generation of NiMH electrode materials, are receiving more and more interest for their high capacity and long cycle life. It is with these electrode materials that the Ovonic Battery Company has developed the NiMH battery with high energy density [5,6]. Therefore, many researchers have focused on the development of Zr-based alloys for EV-NiMH batteries [4–8,11,12].

In the AB_2 Laves phase alloys, where the radius of A atoms are bigger than that of B atoms, the theoretic radius ratio is $R_A/R_B = 1.225$. In these Laves phase alloys there are three types of crystal-structure (C15($MgCu_2$), C14($MgZn_2$) and C36($MgNi_2$)), while so far, only C15($MgCu_2$) cubic structure and C14($MgZn_2$) hexagonal structure are known to absorb hydrogen. Besides the geometric factors, the electronic effects should also be taken into account to demonstrate the stability of Laves phases. The crystalline structure type is relative to the averaged number of outer-electrons n [13]. When $n<4.67$, no Laves phase is formed; when $n=4.67$–5.4, the C15-Laves phase structure formed in Zr-based alloys, but no Laves phase is formed in the Ti-based alloys; when n is between 4.5 and 7.0, the C14-Laves phase structure appears to occur in Zr- and Ti-based alloys. When $n>7$, both of them form the C15 Laves phase again.

A great deal of work has been carried out on Zr-based AB_2 alloys, which were composed of C15, C14-Laves phase and non-Laves phase such as Zr_7Ni_{10}, Zr_9Ni_{11}, ZrNi phase. However these multi-phase materials are vulnerable to corrosion due to the phenomenon of localized micro-cells, which reduces the performance on cycling [14]. Therefore, SAFT (France) has adopted a monophase hydridable alloy for the negative electrode with 'Laves phase' structure of hexagonal C14 type ($MgZn_2$).

The rapid quenching effect from molten alloys such as induced by melt-spinning technique tends to improve the control of hydrogen storage phases while minimizing mirror phases that do not contribute to storage capacity, and possibly form alloys as a single phase. But it is well known that it is difficult to make hyper-stoichiometric AB_2 alloys as single phase because of its limited solid solution range. Therefore, only a few studies of hyper-stoichiometric AB_2 alloys have been reported. However, it has been reported recently that some hyper-stoichiometric Zr-based Laves phase alloys showed excellent hydriding and electrochemical performance compared with that of the stoichiometric alloys [9,15]. In our work, the hyper-stoichiometric Zr-based AB_2 alloys are the two series of $Zr[(NiVMnCo)_{1-y}Sn_y]_{2+\alpha}$ ($y=0$, 0.025, 0.05) and $(Zr_{1-x}Ti_x)[NiVMnCo]_{2+\alpha}$ ($0.05<x\leq 0.15$, $0<\alpha<0.3$).

The object of the present paper is to develop advanced nanocrystalline Zr-based AB_2 hydrogen storage electrode materials for a NiMH battery system used in an electric vehicle, via the high-tech method of complete crystallization method from amorphous solids. The complete crystallization method is an efficient way to produce porosity-free nanocrystalline materials [16,17]. The microstructure, crystal-structure and electrochemical properties of nanocrystalline alloys were compared with those polycrystalline alloys obtained by conventional induction melting with the same alloy composition. We hope that our work will contribute to development and commercialization of high-performance NiMH batteries for electric vehicles (PEV and HEV) in China.

2. Experimental details

Alloy samples of $Zr[(NiVMnCo)_{1-y}Sn_y]_{2+\alpha}$ ($y=0$, 0.025, 0.05) and $(Zr_{1-x}Ti_x)[NiVMnCo]_{2+\alpha}$ ($0.05<x<0.15$, $0<\alpha<0.3$), were prepared by vacuum induction melting under the purified argon atmosphere. Then the as-cast alloy pieces were mechanically ground. One part was ground to 200 mesh alloy powders, the other part was rapidly solidified into alloy flakes which were prepared by the 5T Advanced Melt Spinner made in American Marko Materials, Inc. and ground to 200 mesh powders.

In order to discuss easily, the samples were named: $QAB_2^{\#}-1$ ($y=0$), $QAB_2^{\#}-2$ ($y=0.025$), $QAB_2^{\#}-3$ ($y=0.05$) and $QAB_2^{\#}-4$ (including Ti) for quickly quenched states; $AB_2^{\#}-1$, $AB_2^{\#}-2$, $AB_2^{\#}-3$ and $AB_2^{\#}-4$ for relevant as-cast states; while quenched and heat treated: $QHTAB_2^{\#}-1$, $QHTAB_2^{\#}-2$, $QHTAB_2^{\#}-3$ and $QHTAB_2^{\#}-4$.

The electrochemical properties were determined using a BT-2043 battery testing system made by Arbin Company, USA. The process of sample preparation was as follows.

(a) Prepared total weight of 3.0000 g powder of hydrogen storage alloy and Ni with the ratio of 1:3.
(b) The powder was cold-pressed into a 25-mm-diameter electrode pellet by a pressure of 624 MPa.
(c) The pellet was sandwiched between two NiOOH/$Ni(OH)_2$ electrodes with excessive capacity, and then put into a beaker with 6 M KOH solution.

The discharge capacity measurement was controlled at 298±1 K. The sample was charged at a current density of 60 mA g^{-1} for 8 h, rested for 5 min, and then discharged at the same current density to a cut-off voltage of 1.0 V.

The charge–discharge cycle life had been measured after the sample was activated for 10 cycles at a charge–discharge current density of 60 mA g^{-1}. The sample was charged for 1.75 h at a charge current density of 120 mA g^{-1} and discharged for 1.25 h at the same current density. A full charge–discharge (at 60 mA g^{-1}) was controlled every 30 cycles.

After the sample had been activated for 10 cycles at the charge–discharge current density of 60 mA g^{-1}, the high-rate discharge ability (HRDA) was determined by the following equation

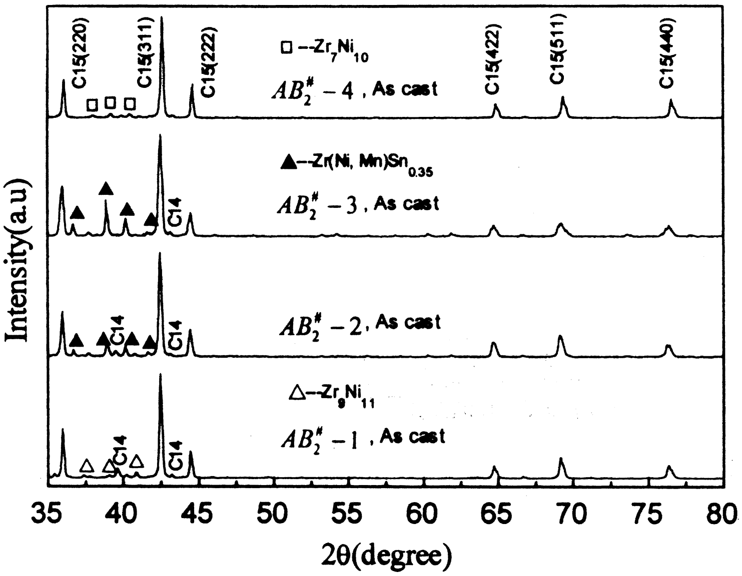

Fig. 1. X-ray diffraction patterns of four as-cast polycrystalline AB_2 alloys.

$$\mathrm{HRDA}(\%) = \frac{C_{600}}{C_{600} + C_{60}} \times 100$$

where C_{600} is the discharge capacity at 600 mA g^{-1}, C_{60} is the residual discharge capacity determined at 60 mA g^{-1} by resting 10 min after the measurement of C_{600}.

The crystal structures of the alloys were confirmed by X-ray diffraction (XRD) and by transmission electron microscopy (TEM). XRD was carried on the Rigaku D/max-γ_A diffraction device, Cu Kα radiation and optical filtering with the graphite monochromator. TEM was on a Philips EM420 type transmission electron microscope.

In order to study the microstructure of the alloys, after polishing and etching of the alloy sample surface, SEI and BEI were observed on the S360 type SEM from Cambridge Instrument Ltd., and EDX carried out at the same time. Crystallization temperatures were measured with a differential thermal analyzer (DTA) at the heating rate of 1.67×10^{-1} K s^{-1} (10 K min^{-1}). Amorphous phases were annealed at 773, 973, 1173 K for 3.6 ks to crystallize.

3. Results and discussion

3.1. As-cast polycrystalline alloys

3.1.1. Crystal-structure

Fig. 1 shows the X-ray diffraction patterns of four as-cast polycrystalline AB_2 alloys. From the patterns it is clear that the AB_2 alloys consist of a large amount of cubic C15 Laves phase, along with a little hexagonal C14 Laves phase and non-Laves phase. In the AB_2 alloy #1, the non-Laves phase is Zr_9Ni_{11}. Large amounts of non-Laves phase in alloy #2 and alloy #3 is $Zr(NiMn)Sn_{0.35}$, while the non-Laves phase in alloy #4 is Zr_7Ni_{10}.

3.1.2. Metallurgical microstructure

The results of SEM observations are presented in Fig. 2. It shows that the microstructure of $AB_2^{\#}-1$ is similar to $AB_2^{\#}-4$, with white phases scattering on the gray matrix. The only difference between them is that the white phases contain a few gray phases in $AB_2^{\#}-1$. The microstructures

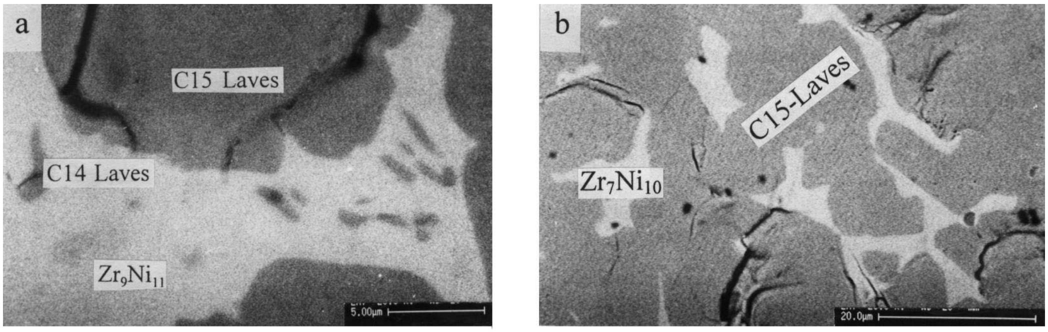

Fig. 2. SEM micrographs of the as-cast polycrystalline AB_2 alloys (a) $AB_2^{\#}-1$; (b) $AB_2^{\#}-4$.

Table 1
SEM-EDX analysis (at.%) of the composition of the alloys

Alloy $AB_2^{\#}-1$	Zr	Ni	V	Mn	Co	O		Phase
Gray region (matrix)	32.67	32.84	8.29	22.19	4.01	–		C15-Laves
White region	44.49	50.01	0.57	3.33	1.60	–		Zr_9Ni_{11}
Gray in the white	35.94	42.24	3.34	15.80	2.68	–		C14-Laves
Dark dot	29.15	1.44	0.10	0.65	0.02	68.6		α-ZrO_2
Alloy $AB_2^{\#}-2$	Zr	Ni	V	Mn	Co	Sn		Phase
Gray region (matrix)	34.25	29.64	10.16	21.16	4.05	0.74		C15-Laves
Lutectic structure region	44.66	33.50	0.37	3.75	1.09	16.63		$Zr(NiMn)Sn_{0.35}$
Alloy $AB_2^{\#}-3$	Zr	Ni	V	Mn	Co	Sn		Phase
Gray region (matrix)	32.17	31.84	9.90	20.63	4.48	1.44		C15-Laves
Lutectic structure region	41.45	34.80	0.37	3.75	1.09	16.63		$Zr(NiMn)Sn_{0.35}$
Honeycomb-like structure region	41.60	37.39	0.04	4.88	1.28	14.81		$Zr(NiMn)Sn_{0.35}$
Alloy $AB_2^{\#}-4$	Zr	Ni	V	Mn	Co	O	Ti	Phase
Gray region (matrix)	29.84	35.04	7.38	20.55	4.08	–	3.10	C15-Laves
White region	37.18	54.15	–	2.75	1.09	–	4.83	Zr_7Ni_{10}
Dark dot	37.22	6.33	–	1.04	0.23	54.59	0.59	α-ZrO_2

of $AB_2^{\#}-2$ and $AB_2^{\#}-3$ are alike with white phases scattering on the gray matrix, while in $AB_2^{\#}-3$ there is some honeycomb-like structure. A few dark dots exist in all of the four alloys. According to the SEM-EDX analysis results (in Table 1), the gray matrix is C15-Laves phase, the white zone is Zr_9Ni_{11} ($AB_2^{\#}-1$) and Zr_7Ni_{10} ($AB_2^{\#}-4$), the brown region in the white zone is C14-Laves phase, the dark dot is α-ZrO_2. The test agrees well with earlier results [8].

3.1.3. Electrochemical properties

Fig. 3 shows the variation in discharge capacity with the number of charge–discharge cycles for the as-cast polycrystalline AB_2 electrodes. It can be clearly seen that the discharge capacities of $AB_2^{\#}-1$ and $AB_2^{\#}-4$ are obviously higher than those of the other two alloys. Further observation reveals that the capacity of $AB_2^{\#}-4$ is slightly higher than that of $AB_2^{\#}-1$, while the capacity of $AB_2^{\#}-3$ is well below that of $AB_2^{\#}-2$. In the Zr-based AB_2 Laves phase hydrogen storage alloys, the Zr_7Ni_{10} and Zr_9Ni_{11} phase have a high hydrogen capacity in solid–gas reaction (370 mAh g^{-1} and 340 mAh g^{-1}) but a small capacity studied in the electrochemically discharged capacity are 50 mAh g^{-1} and 95 mAh g^{-1}, respectively [18]. However, the coexistence of the two phases (Laves phase and non-Laves-phase) in a metallurgical compound leads to the charge and discharge of Laves phases (C15, C14) through the non-phases (Zr_7Ni_{10}, Zr_9Ni_{11}). Hydrogen atom diffusion between the Laves phases and this non-Laves phase through grain boundaries and interface proceeds easily. Moreover, the non-Laves phases can be hydrided. Therefore, the combined contribution of the above two phases should enable the electrode to possess both good activation properties and high electrochemical capacity. The large

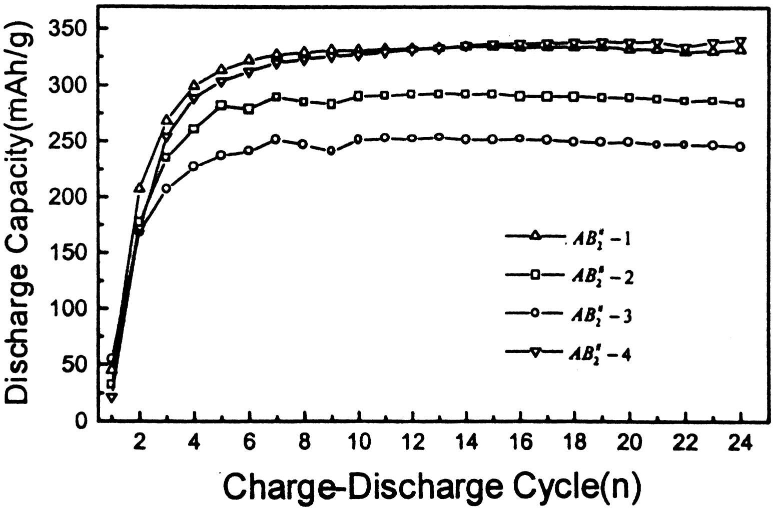

Fig. 3. Variation in discharge capacity with number of charge–discharge cycles for the as-cast polycrystalline alloys

Table 2
The results of high-rate discharge ability test of the as-cast polycrystalline alloys

Alloys	AB$_2^{\#}-1$	AB$_2^{\#}-4$
C_{600} (mAh g^{-1})	205	245
C_{60} (mAh g^{-1})	119	95.2
$C_{600}/(C_{600}+C_{60})$ (%)	63.3	72.0

amount of non-Laves phase in the two alloys (containing Sn) is Zr(NiMn)Sn$_{0.35}$, and the eutectic structure is not favorable for hydrogen absorbability. Since the AB$_2^{\#}-3$ contains more Sn, its discharge capacity is much lower. The highest discharge capacity of AB$_2^{\#}-4$ may be contributed to the substitution of Ti+Co, which reduces the stability of the hydrides [8]. It is in concurrence with the results of the high-rate discharge test (see Table 2).

The high rate of dischargeability of the AB$_2^{\#}-4$ alloy with respect to the amount of substituted Ti may be due to the formation of a Ti-oxide film on the metal hydride surface, which is more porous than the Zr-oxide film and lets the hydrogen atom penetrate easily through its porous surface [11]. A mixture of Ti- and Zr-oxides should be much less of a barrier to hydrogen penetration compared with a pure Zr-oxide layer [19].

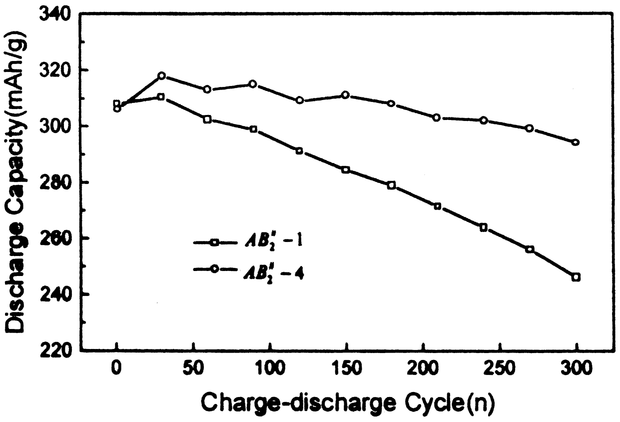

Fig. 4. The curves of charge–discharge cycle life for AB$_2^{\#}-1$ and AB$_2^{\#}-4$.

Fig. 4 is the plot of charge–discharge cycle-life for AB$_2^{\#}-1$ and AB$_2^{\#}-4$, which exhibit higher discharge capacities. It can be seen that the cycle life of AB$_2^{\#}-4$ is obviously longer than that of AB$_2^{\#}-1$. Although the reason for this phenomenon is not clear, it is suggested that the more stable Ti oxide protects the electrode during the charge–discharge cycles.

3.2. Quenched state alloys

3.2.1. X-ray diffraction analysis

Fig. 5 shows the X-ray diffraction patterns of the four quenched alloys. After quenching, the microstructures of AB$_2^{\#}-1$ and AB$_2^{\#}-4$ have basically turned into C15 Laves single phase, while non-Laves phase Zr(NiMn)Sn$_{0.35}$ still exists in AB$_2^{\#}-2$ and AB$_2^{\#}-3$. At the high cooling rate (10^5–10^6 K s^{-1}) some amorphous phase appears after quenching. It can be seen from the widening of the diffraction peaks. It is also confirmed by DTA and TEM analysis.

3.2.2. TEM analysis

The transmission electron microscopy (TEM) and correlated electron diffraction patterns of QAB$_2^{\#}-4$ alloy is presented in Fig. 6. It was clearly observed that part of the structure has turned into amorphous phase after quenching.

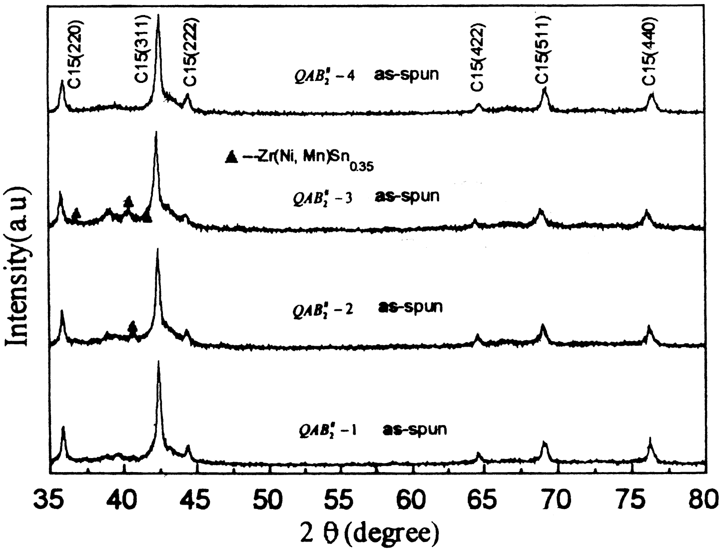

Fig. 5. X-ray diffraction patterns of the four quenched alloys.

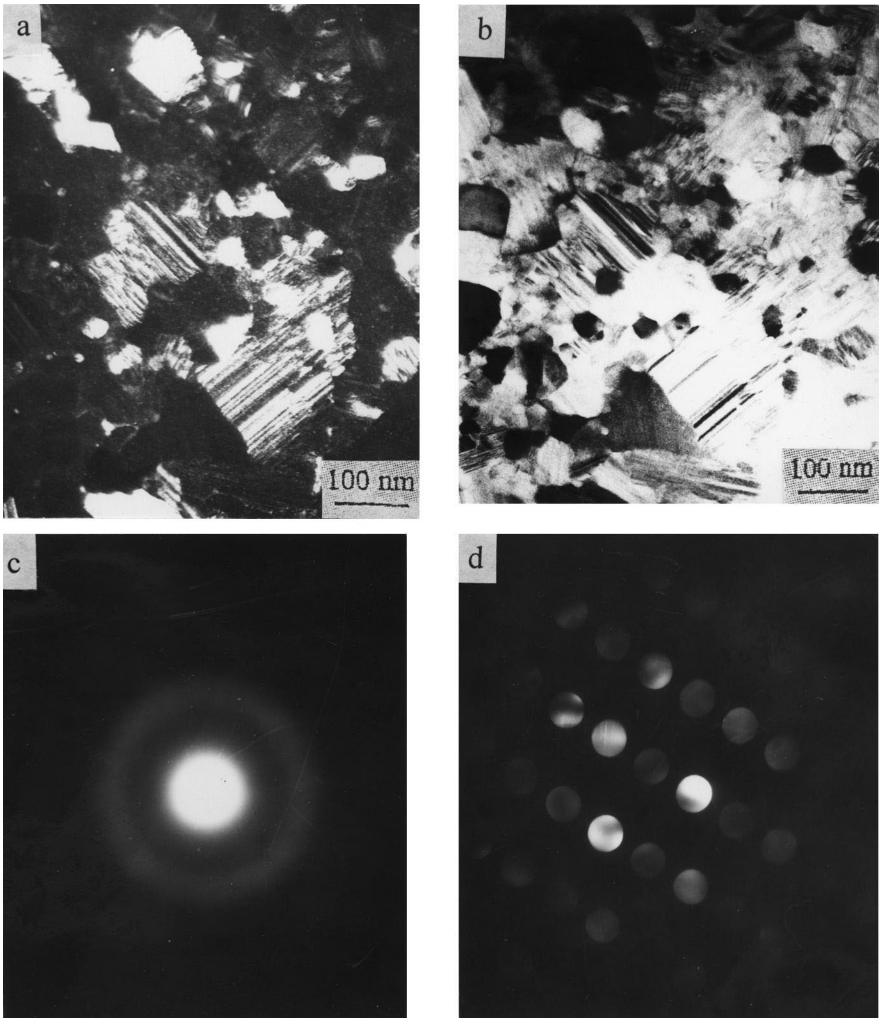

Fig. 6. Transmission electron micrographs of $QAB_2^{\#}-4$ alloy. (a) DF appearance; (b) BF appearance; (c) SAED pattern of the white area; (d) SAED pattern of the dark area in BF.

3.2.3. *Electrochemical property*

Fig. 7 illustrates the variation in discharge capacity with the number of charge–discharge cycles for electrodes of quenched alloys. These electrodes exhibit low discharge capacities and poor activation behavior. This could be due to the decreased number of tetrahedral interstitial sites (TIS) that can be occupied by hydrogen atoms, some part of the alloys having turned into amorphous phase after quenching. And the capacity for hydrogen absorbtion decreases as a result. At the same time, hydrogen atom diffusion ability in such alloys is relatively lower, which is also not favorable to the activation behavior of the alloy electrodes.

3.3. *Nanocrystalline alloys*

From the above results, it is clear that quenched alloys without heat-treatment are not suitable to be used as electrode materials for a NiMH battery, as far as discharge capacity and activation behavior are concerned. In order to eliminate the amorphous phase in the alloys and promote their hydrogen storage capacity, quenched alloys were annealed at 773 K, 973 K, and 1173 K, respectively, with reference to the two transition temperatures in the DTS curve of QAB_2-1 alloy (Fig. 8).

3.3.1. *Crystal structure*

Fig. 9 shows the X-ray diffraction patterns of the four quenched alloys after heat-treatment. The amorphous phase disappears completely in the alloy after annealing at 1173 K, substituted by nanocrystalline diffraction patterns. The alloys still have C15 Laves single-phase, while in QAB_2-2 and QAB_2-3 there is some non-Laves phase $Zr(NiMn)Sn_{0.35}$.

3.3.2. *Metallurgical microstructure*

Fig. 10 shows transmission electron micrographs and SAED patterns of $QAB_2^{\#}-4$ after heat-treatment. It was clearly observed that the grain size is in the nanometre-sized range (<100 nm), and correspondingly nanocrystal-

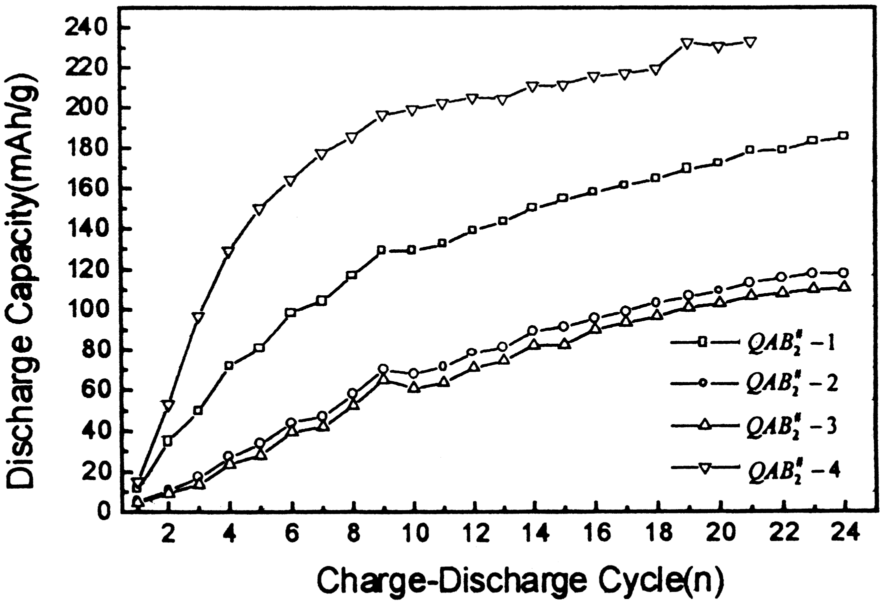

Fig. 7. Variation in discharge capacity with the number of charge–discharge cycles for the electrodes of quenched alloys.

line materials were directly obtained by melt-spinning and vacuum annealing treatment. The nanocrystalline alloys have this special microstructure composed of high-density interface phase and random-oriented grains. When the annealing temperature is 773 K, the diffraction pattern of the alloy appears as bright continuous rings, indicating that the alloy still consists of amorphous phase. The diffraction pattern of the alloy annealed at 973 K changes into discontinuous rings, indicating that besides a small amount of amorphous phase, the rest has turned nanocrystalline. When the annealing temperature is 1173 K, the diffraction pattern is discontinuous rings consisting of scattered dots, which shows that the alloy has turned nanocrystalline completely. Grain sizes of the annealed alloys estimated by TEM micrographs are listed in Table 3. The grain sizes are several nanometres to several dozens of nanometres. The average grain sizes were measured within a wide annealing temperature range of 773 to 1173 K. They increase with increasing temperature in the range of 773 to 1173 K, and reach a minimum value of about 80 nm at about 1173 K.

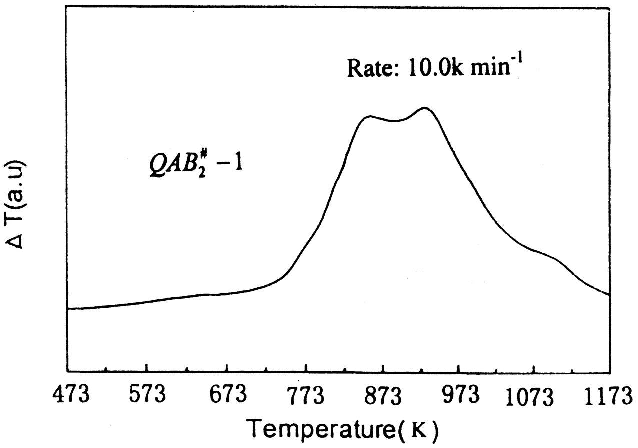

Fig. 8. DTS curve of QAB$_2^\#-1$ alloy.

3.3.3. Electrochemical properties

Fig. 11 demonstrates the variation in discharge capacity with the number of charge–discharge cycles for the four alloys before/after quenching and before/after annealing. It is shown that annealing can increase the discharge capacity of the electrode material, owing to the large amount of hydrogen-accommodating interface in nanometre crystallites. The reasons are as follows: nanocrystalline materials consist of two structural components of (1) nanometre-sized crystallites and (2) grain boundaries of interfaces between the crystallites, which enable many properties of the nanocrystalline materials to be fundamentally different from and frequently superior to those of conventional polycrystals and the amorphous state [20,21]. We emphasize that there are substantially two regions in Zr-based AB$_2$ alloys: the intra-grain region of the crystallites as C15-Laves phase, its inter-grain region. It has been shown that the inter-grain region can act as suitable diffusion paths for hydrogen atoms, the origin for the notable hydriding properties was found to be an intensive formation of an inter-grain region around the intra-grain region composed of the crystallites [22]. Hydro-

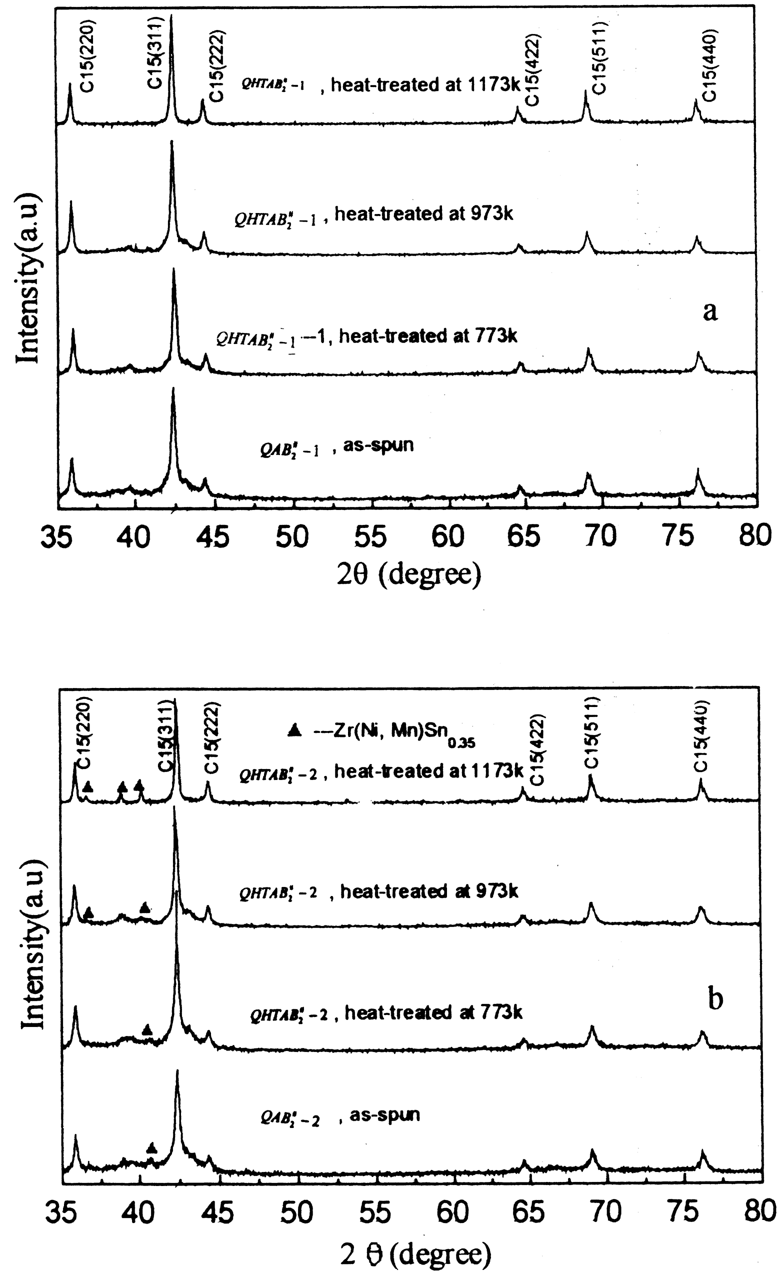

Fig. 9. X-ray diffraction patterns of the four quenched alloys after heat-treatment. (a) $QHTAB_2^{\#}-1$; (b) $QHTAB_2^{\#}-2$; (c) $QHTAB_2^{\#}-3$; (d) $QHTAB_2^{\#}-4$.

gen atoms preferentially dissolving into the inter-grain region relating to the cooperative phenomena between both the intra- and inter-grain regions. Thus, one of the directions for a further improvement of hydriding and dehydriding properties in the Zr-based AB_2 crystallites is to enrich the inter-grain region.

Fig. 12 shows the plot of charge–discharge cycle-life for AB_2-1 and AB_2-4 (as-cast or annealed after quenching), which exhibits higher discharge capacities. Nanocrystalline hydrogen storage electrode materials possess both high discharge capacity and long cycle-life. This may be attributed to two reasons. Firstly, nanocrystalline electrodes have more resistance to pulverization, because the fine grains result in much lower macro-stress during hydrogen-absorbing; secondly, since there are many more interfaces in nanocrystalline materials, the alloy element or oxides at the interfaces could protect the grains more efficiently and slow the corrosion during the charge–discharge process.

Relation between the maximum discharge capacity and

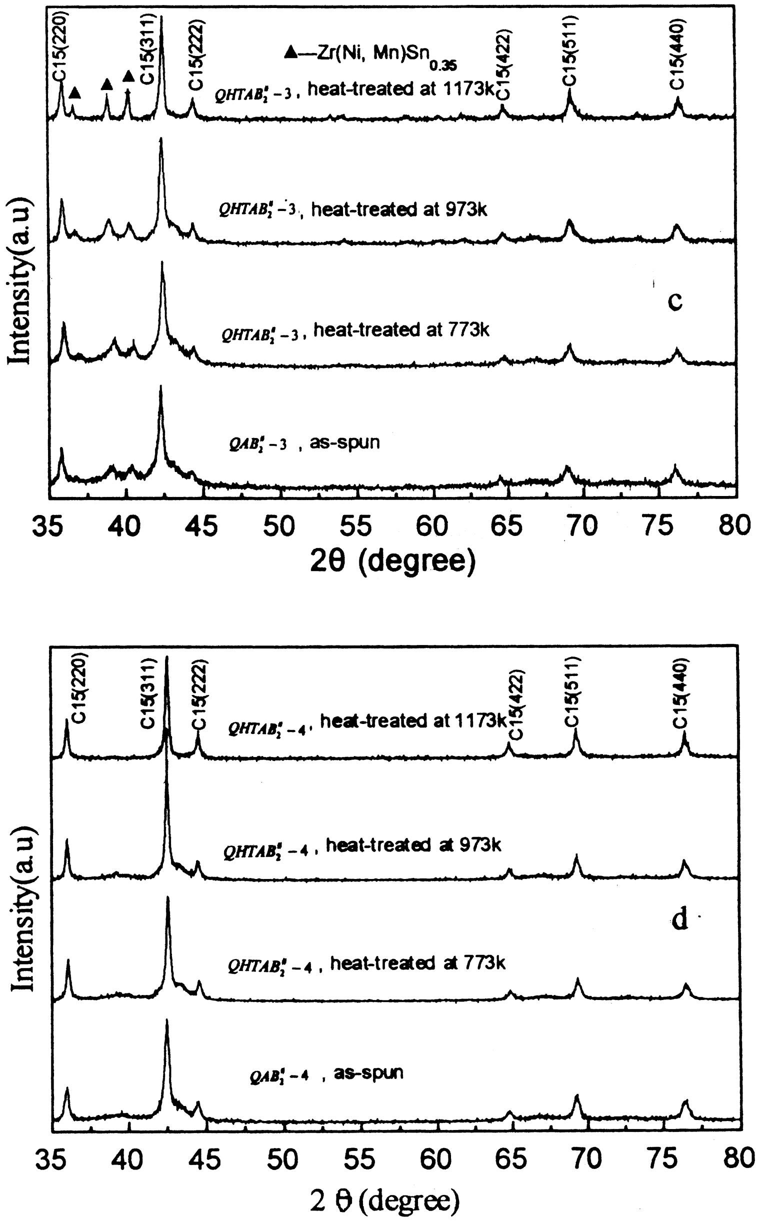

Fig. 9. (*continued*)

metallurgical microstructure and crystal-structure in the alloys are shown in Fig. 13. The maximum discharge capacities were found to depend on the metallurgical microstructure and crystal-structure in the Zr-based AB_2 alloys. The maximum discharge capacity increases in regular order nanocrystalline/C15-Laves single-phase> polycrystalline/multi-phase (Laves and non-Laves)> amorphous state/C15-Laves single-phase.

Due to the special microstructure of interfaces, nanocrystalline materials exhibit unique characters different from those of conventional crystalline or amorphous materials. Research has been performed on the hydrogen-storage behaviors of nanocrystalline Mg, Mg_2Ni, FeTi and $LaNi_5$ [22–25]. According to the above investigation, it is concluded that nanocrystalline hydrogen storage electrode materials are very promising new hydrogen storage electrode materials with high capacity and long cycle life, compared with conventional crystalline materials.

4. Conclusions

1. The metallurgical microstructures and electrochemical properties of four Zr-based Laves phase hydrogen

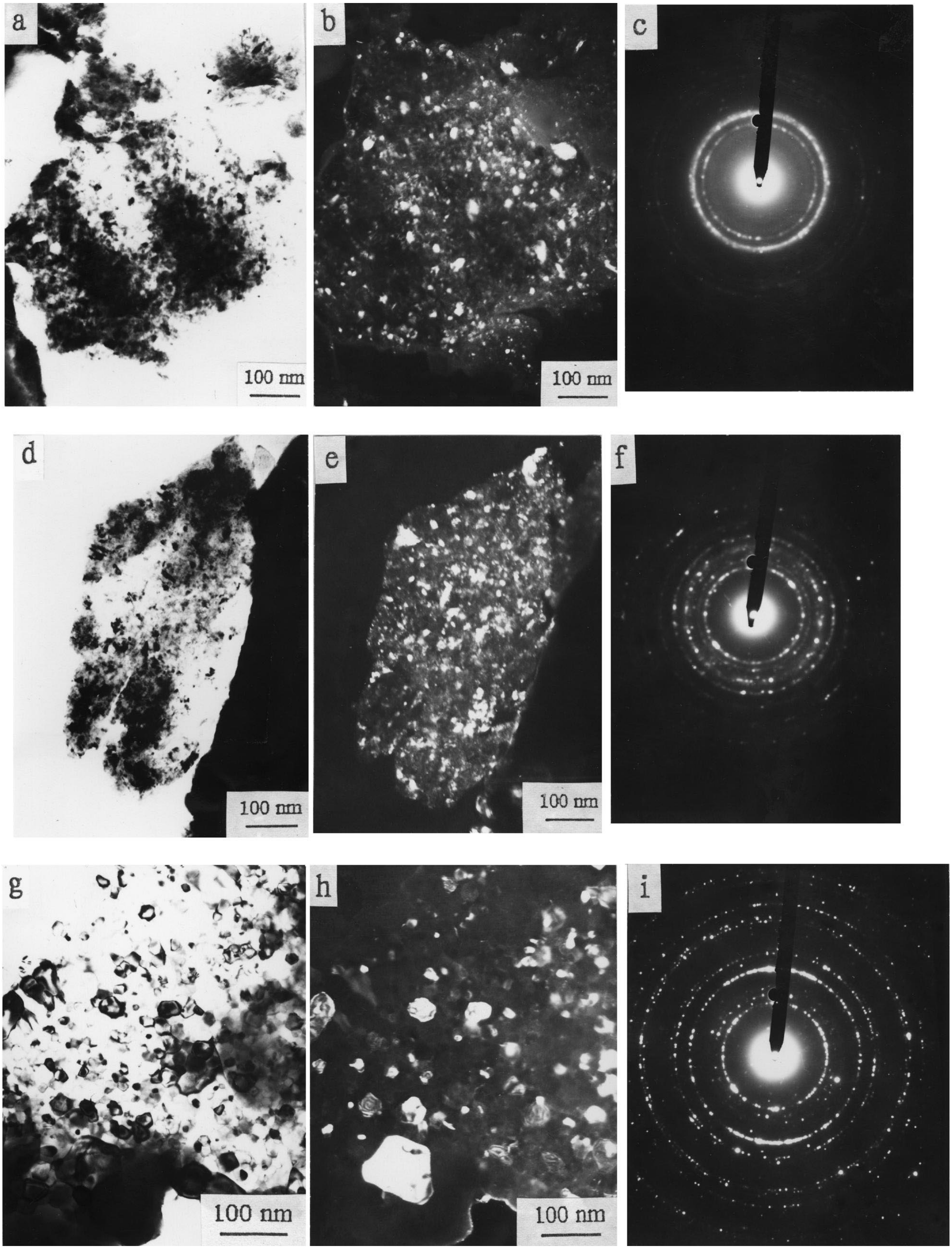

Fig. 10. TEM micrographs and SAED patterns of $\mathrm{QHTAB}_2^{\#}-4$. (a, b, c) Annealing at 773 K; (d, e, f) annealing at 973 K; (g, h, i) annealing at 1173 K; (a, d, g) bright field; (b, e, h) dark field; (c, f, i) SAED patterns.

Table 3
Grain sizes of the annealed alloys estimated by TEM micrographs

Alloys	Annealing temperature/K	Grain sizes/nm	Grain average value/nm
$QAB_2^{\#}-1$	773	1.0–19.0	8.5
	973	1.9–28.6	13.3
	1173	6.7–30.5	18.7
$QAB_2^{\#}-2$	773	1.0–24.4	9.4
	973	1.9–31.1	13.4
	1173	4.8–57.1	18.8
$QAB_2^{\#}-3$	773	1.0–23.8	9.0
	973	4.8–38.1	14.6
	1173	7.6–114.3	48.0
$QAB_2^{\#}-4$	773	4.7–47.6	16.8
	973	7.6–102.8	39.1
	1173	9.5–135.2	47.6

storage alloys were investigated. It was found that the substitution of Ti in small amounts could increase the discharge capacity and prolong the cycle life of the electrode, while the addition of Sn is unfavorable to the discharge capacity.

2. The microstructures and crystal-structures of the polycrystalline alloys consist of cubic C15 Laves phase, hexagonal C14 Laves phase and non-Laves phase (such as Zr_7Ni_{10}, Zr_9Ni_{11}, $Zr(NiMn)Sn_{0.35}$). Nanocrystalline alloy has a special microstructure composed of high-density interface phase and random-oriented grains varying from several nanometres to several dozens of nanometres.
3. Advanced nanocrystalline Zr-based AB_2 hydrogen storage alloys could be obtained from quenched alloys after annealing. As a result, the discharge capacity of the electrodes was greatly increased ($>$370 mAh g^{-1}) and the cycle life was also prolonged (the decrease of capacity was only 3% after 300 cycles).
4. On the metallurgical microstructure and crystal-structure in the Zr-based AB_2 alloys; the maximum discharge capacity increases in regular order nanocrystalline/C15-Laves single phase$>$ polycrystalline/multi-phases (Laves and non-Laves)$>$ amorphous state/C15-Laves single-phase.
5. The complete crystallization method from amorphous solids is an effective way to get nano-structured AB_2 electrode materials with excellent performances for high-energy-density batteries in pure electric vehicles (PEV) and hybrid electric vehicles (HEV).

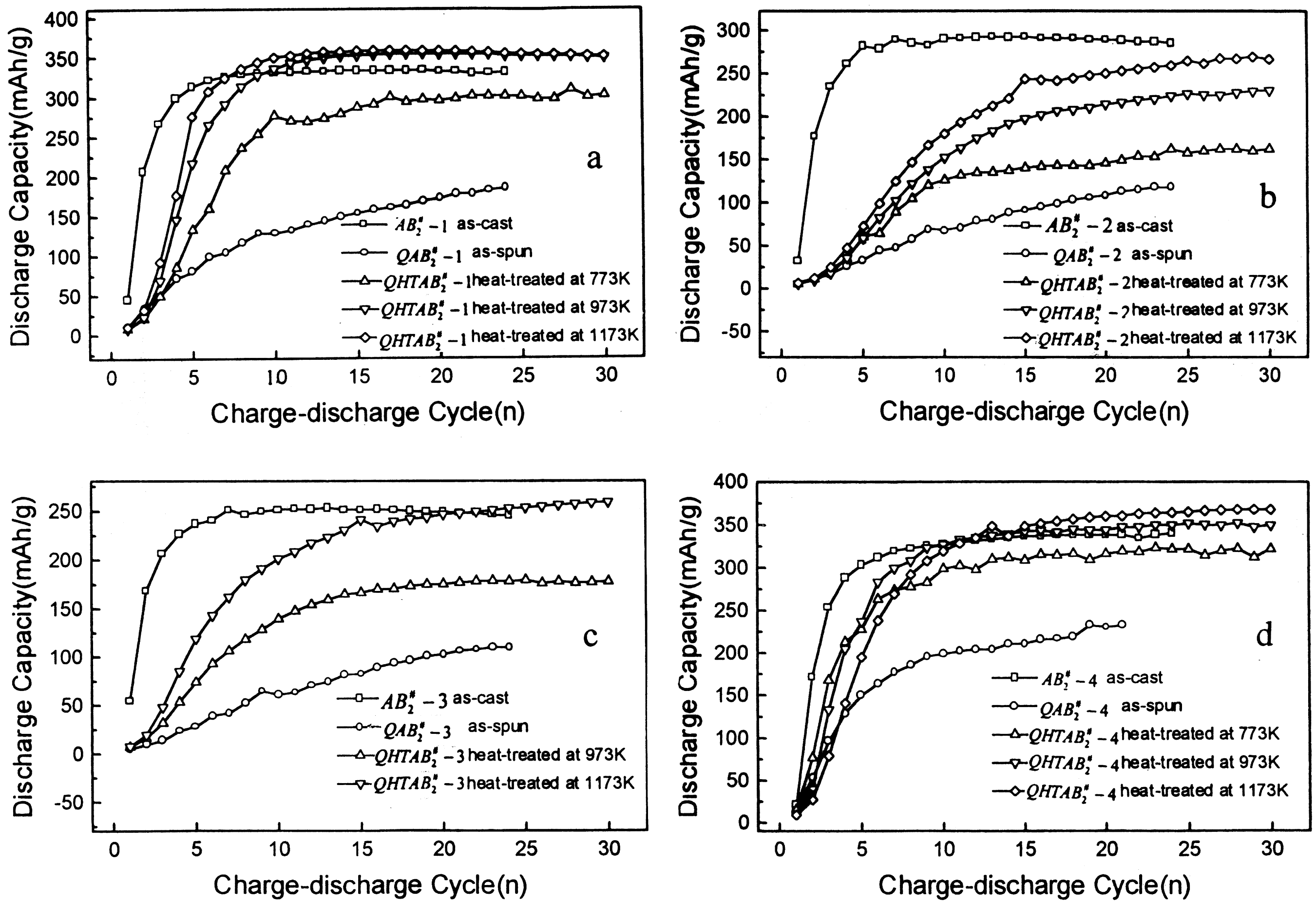

Fig. 11. Variation in discharge capacity with the number of charge–discharge cycles for quenching and before/after annealing. (a) $QHTAB_2-1$; (b) $QHTAB_2-2$; (c) $QHTAB_2-3$; (d) $QHTAB_2-4$.

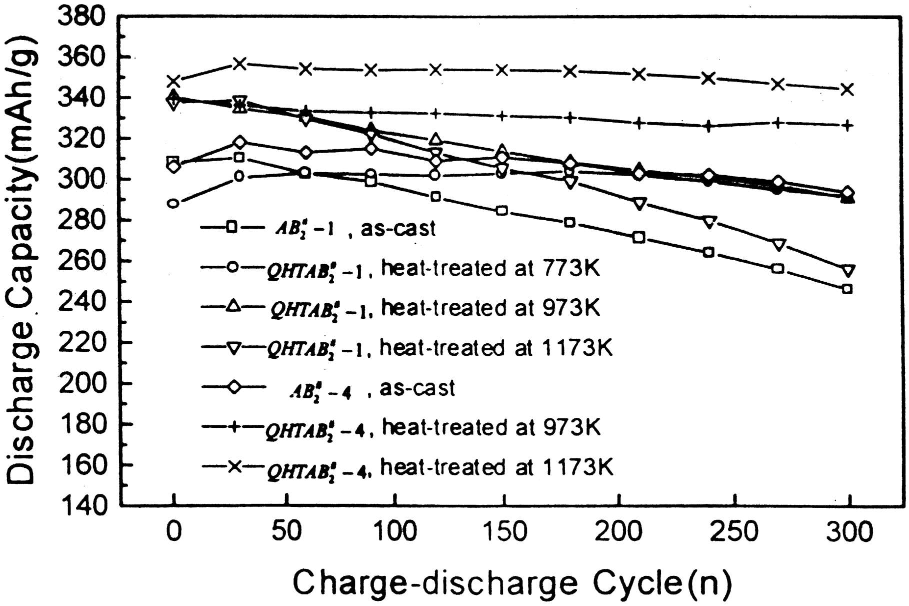

Fig. 12. Charge–discharge cycle-life for AB_2-1 and AB_2-4 (as-cast or annealed after quenching).

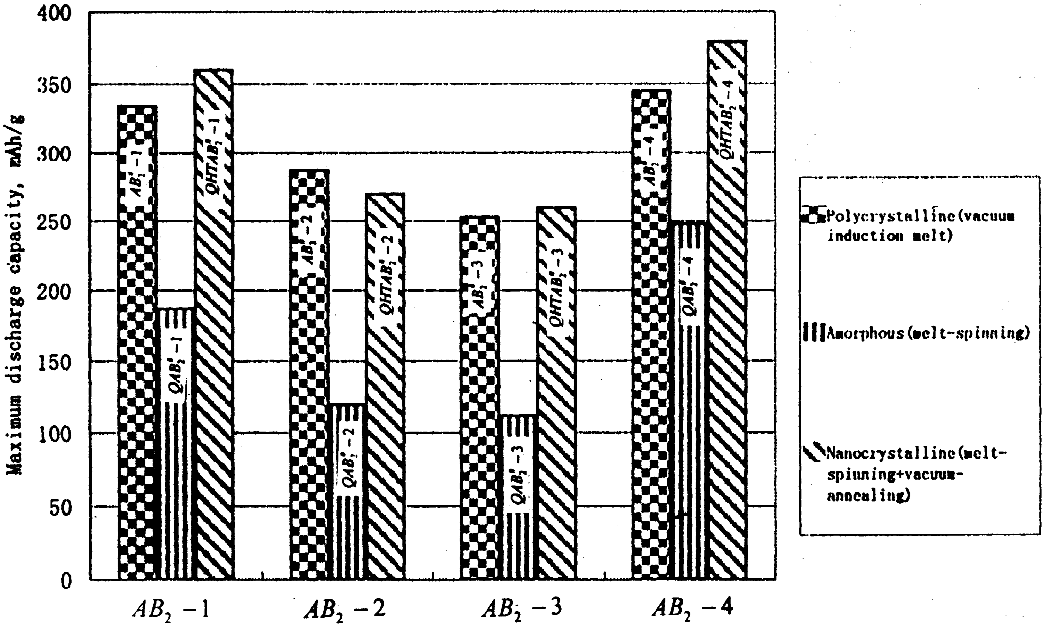

Fig. 13. Relation between the maximum discharge capacity and metallurgical microstructure/crystal-structure in the alloys.

Acknowledgements

This work was supported by the National Advanced Materials Committee of China (product no. 715-004-0233).

References

[1] T. Kimura, M. Ikoma, K. Kanamanl, in: The 15th International Electric Vehicle Symposium, Belgium, 1998, p. 69.

[2] N. Fujioka, M. Ikoma, in: The 15th International Electric Vehicle Symposium, Belgium, 1998, p. 71.

[3] D. Corrigan, P. Gow, I. Menjak, S. Venkatesan, S. Dhar, R. Stempel, S. Oveshinsky, in: The 15th International Electric Vehicle Symposium, Belgium, 1998, p. 365.

[4] P. Gifford, V. Hellmann, J. Adams, in: The 15th International Electric Vehicle Symposium, Belgium, 1998, p. 107.

[5] S.K. Dhar, S.R. Ovshinsky, P.R. Gifford, D.A. Corrigan, M.A. Fetcenko, S. Venkatesan, J. Power Sources 65 (1997) 1–7.

[6] S.R. Ovshinsky, M.A. Fetcenko, in: 185th Meeting of the Electrochemical Society, San Francisco, CA, May, 1994.

[7] S.R. Ovshinsky, M.F. Fetcenko, A. Holland, K. Dean, D. Fillmore, US Patent 5,536,591, Sept. 24, 1996.

[8] S.R. Ovshinsky, M.A. Fetcanko, J. Ross, Science 260 (1990) 176.
[9] D.-M. Kim, S.-W. Jeon, T.-Y. Lee, J. Alloys Comp. 279 (1998) 209–214.
[10] R. Mishima, H. Miyamcera, T. Sakai, N. Kuriyama, H. Ishikawa, I. Uehara, J. Alloys Comp. 192 (1993) 176–178.
[11] J.S. Kim, C.H. Paik, W.I. Cho, B.W. Cho, K.S. Yun, S.J. Kim, J. Power Sources 75 (1998) 1–8.
[12] A. Zuttel, F. Meli, L. Schlapbach, J. Alloys Comp. 231 (1995) 645–649.
[13] R.P. Elliott, W. Rostoker, Trans. ASM 6 (1958) 617.
[14] B. Knosp, J. Bouet, M. Mimoun, D. Gicquel, U.P. Patent 56,26,987, May 6, 1997.
[15] S. Wakao, H. Sawa, J. Furukawa, J. Less-Common Metals 172–174 (1991) 1219.
[16] M.L. Sui, L.Y. Xiong, W. Deng, K. Lu, S. Patu, Y.Z. He, J. Appl. Phys. 69 (1991) 4451.
[17] M.L. Sui, L.Y. Xiong, W. Deng, K. Lu, S. Patu, Y.Z. He, Mater. Sci. Forum 105–110 (1992) 1299.
[18] J.M. Joubert, M. Latroche, A. Percheron-Guegan, J. Boccet, J. Alloys Comp. 240 (1996) 219–228.
[19] J.O. Strom-Olsen, Y. Zhao, D.H. Ryan, J. Less-Common Metals 172–174 (1991) 922.
[20] H. Gleiter, Prog. Mater. Sci. 33 (1989) 223.
[21] C. Suryanargana, Int. Mater. Rev. 40 (1995) 41–46.
[22] S. Orimo, K. Ikeda, H. Fujii, Y. Fujlkawa, Y. Kitano, K. Yamamoto, Acta Mater. 45 (1997) 2271–2278.
[23] L. Zaluski, A. Zaluska, J.O. Strom-olsen, J. Alloys Comp. 253–254 (1997) 70.
[24] S. Orimo, H. Fuji, K. Ikeda, Acta Mater. 45 (1997) 331.
[25] S. Orimo, H. Fuji, J. Alloys Comp. 232 (1996) L16.